

Article

Hierarchically Electrodeposited Nickel/Graphene Coatings for Improved Corrosion Resistance of Ni Foam Flow Field in PEMFC

Yuzhen Xia ¹, Qibin Zuo ¹, Chuanfu Sun ¹, Guilin Hu ^{1,*} and Baizeng Fang ^{2,*}

¹ School of Mechanical and Energy Engineering, Zhejiang University of Science and Technology, Hangzhou 310023, China; yuzhen.xia@zust.edu.cn (Y.X.); zuoqibin06@163.com (Q.Z.); 222301855023@zust.edu.cn (C.S.)

² School of Chemical Engineering and Energy Technology, Dongguan University of Technology, Dongguan 523808, China

* Correspondence: enehgl@163.com (G.H.); baizengfang@163.com (B.F.)

Abstract: Metal foams are promising materials for the flow fields of proton exchange membrane fuel cells (PEMFCs) because of excellent mass transport characteristics and high electronic conductivity. To resolve the corrosion problem in the acidic environment under high temperature, nickel/graphene (Ni/G) composite coatings with hierarchical structures were electrodeposited on the surface of Ni foam. The effect of grain size and the distribution in the double layer was discussed. It was found that Ni/G5-10, with larger inner size and middle outer size, exhibited the best corrosion performance. Meanwhile, the corrosion current in the Tafel plots and the steady current density in constant potential analysis was lower than that obtained under steady and gradient currents. Combined with the results of XRD, XPS, and SEM, it was proven that a uniform and dense protective film was produced during the two-step electrodeposition. Moreover, the ICR value was 8.820 mΩ·cm², which met the requirement of 2025 DOE.

Keywords: PEMFC; metal foam; flow field; electrodeposition; corrosion resistance; nickel/graphene composite



Citation: Xia, Y.; Zuo, Q.; Sun, C.; Hu, G.; Fang, B. Hierarchically Electrodeposited Nickel/Graphene Coatings for Improved Corrosion Resistance of Ni Foam Flow Field in PEMFC. *Inorganics* **2024**, *12*, 293. <https://doi.org/10.3390/inorganics12110293>

Academic Editor: Antonino Gulino

Received: 30 September 2024

Revised: 7 November 2024

Accepted: 12 November 2024

Published: 14 November 2024



Copyright: © 2024 by the authors. Licensee MDPI, Basel, Switzerland. This article is an open access article distributed under the terms and conditions of the Creative Commons Attribution (CC BY) license (<https://creativecommons.org/licenses/by/4.0/>).

1. Introduction

With the increasing global demand for renewable energy and low-carbon technologies [1,2], fuel cells, as an efficient and environmentally friendly energy conversion technology, are receiving increasing attention. Fuel cells directly convert chemical energy into electrical energy during operation, with water as the only byproduct [3]. Among various types of fuel cells, proton exchange membrane fuel cells (PEMFCs) are favored for their high energy conversion efficiency, rapid start-up response, and low-temperature operation [4,5].

Among the main components of PEMFCs, the bipolar plate (BP) accounts for approximately 80% of the total mass and 45% of the cost, serving essential functions in mass transport, water management, and as a mechanical support in the stack [6,7]. Currently, the materials commonly used for bipolar plates (BPs) include graphite, composite materials, and metals. Graphite, as the first material developed for BPs, possesses good electrical conductivity and corrosion resistance; however, it suffers from low mechanical strength and processing difficulties [8,9]. Composite materials combine lightweight properties with excellent conductivity, making them suitable for high-performance applications [10–12]. Nonetheless, existing composite BPs face challenges such as high interfacial contact resistance and elevated costs. In contrast, metallic BPs offer advantages such as good mechanical properties, electrical conductivity, thermal conductivity, and ease of processing, making them a primary choice for BPs [9]. However, under the high-temperature and acidic operating conditions of PEMFCs, metallic materials are prone to corrosion, releasing corrosive metal ions that adversely affect fuel cell performance. Therefore, the introduction of protective coatings to enhance corrosion resistance is crucial [13,14].

Noble metal coatings exhibit excellent corrosion resistance and electrical conductivity; however, their high cost limits widespread application [15]. Consequently, non-noble metal coating materials such as tin (Sn) [16] and nickel (Ni) [17] are receiving increasing attention. For instance, Kim et al. [18] prepared a pure niobium (Nb) coating on a 316 L stainless steel substrate using pulsed direct current magnetron sputtering. Their study revealed that the Nb coating significantly improved the corrosion behavior of the substrate, increasing polarization resistance and reducing corrosion rate by more than 100 times and 50 times, respectively. Kumaravel et al. [19] applied nickel coatings on weathering steel via electroplating, finding that the Ni-coated samples exhibited the lowest corrosion rate when compared to copper and zinc coatings. Wang et al. [20] developed a Ni/Sn composite coating on nickel foam through electrodeposition, which showed no significant pitting after 8 h of corrosion testing compared to the uncoated samples.

Additionally, an increasing number of non-metal coatings are being used in corrosion-resistant coatings [19]. Among these, graphene is gaining traction as a protective coating due to its unique chemical inertness and impermeability [21]. Lee et al. [22] prepared tin, gold, and nanoscale graphene coatings on porous nickel foam, and through Tafel analysis at 80 °C, they found that the graphene-coated nickel foam exhibited the lowest corrosion current density ($0.65 \mu\text{A}/\text{cm}^2$) and a corrosion potential of -0.22 V . Compared to the other two materials, the performance of the graphene coating is superior. Graphene coatings were prepared on titanium-based bipolar plates, which demonstrated significantly enhanced corrosion resistance and stability in PEMFC environments [23,24]. Feng et al. [25] utilized chemical vapor deposition to create vertically aligned graphene coatings on titanium substrates, achieving a corrosion rate reduction in one to two orders of magnitude and a decrease in interfacial contact resistance (ICR) by approximately 100 times compared to uncoated samples.

Graphene–metal composite coatings not only addressed the limitations of single-layer coatings but also reduced costs and improved mechanical stability [26,27]. Rekha et al. [28] electrodeposited Cr–graphene composite coatings on low-carbon steel substrates and conducted corrosion studies using a 3.5% NaCl solution as the electrolytic medium. Their findings revealed an 80.4% reduction in corrosion current and a 72.8% decrease in ICR, significantly enhancing both corrosion resistance and conductivity compared to pure chromium coatings. Punith Kumar et al. [29] prepared Zn–graphene composite coatings through electrodeposition and conducted experiments in a 3.5% NaCl solution. The results indicated that the Zn–graphene coatings exhibited smaller grain sizes and fewer surface defects, leading to enhanced corrosion resistance. Abdul et al. [30] also developed Ni–graphene composite coatings through electrodeposition, investigating the effects of different deposition temperatures on coating performance, with optimal corrosion resistance achieved at 45 °C in a 3.5% NaCl solution. Sun et al. [31] prepared a Ni–graphene composite coating by direct current electrodeposition. Under the test condition of $\text{pH} = 3$, the coating showed good corrosion resistance and stability. Electrodeposition is widely used as a low-cost and easy-to-control coating method. In the process of electrodeposition, the larger the current, the smaller the particles.

Metal foam is used as the flow field to replace traditional BP plates with ribs and channels because of lightweight advantages and high mass transfer efficiency. However, it suffers more severe corrosion issues in the operating environment on account of high temperatures and the presence of acids. Meanwhile, due to the complex internal structure and high surface roughness, the electrodeposition mechanism is different from that on the flat plate. In this work, nickel/graphene (Ni/G) composite coatings with a hierarchical structure are employed by the electrodeposition method. While a larger grain size is obtained under a lower electrodeposition current, the coatings with various size distributions are compared. Their physical properties are analyzed along with their impact on corrosion resistance, ultimately identifying the coating with optimal performance.

2. Results and Discussions

2.1. XRD Analysis

The XRD spectrum of the Ni/G composite coating is shown in Figure 1. The spectrum exhibited three main diffraction peaks at 2θ values of 44.4° , 51.8° , and 76.3° , corresponding to the Ni (111), (200), and (220) planes, respectively, which closely matched the reference pattern for the face-centered cubic nickel. Each coating displayed a strong Ni (111) peak, indicating that during the deposition process, nickel tended to grow preferentially in the (111) orientation [32].

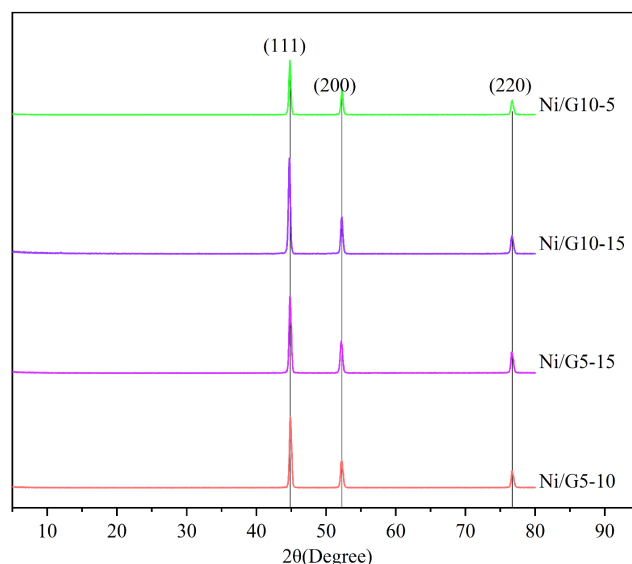


Figure 1. XRD patterns of composite coatings.

Using the Scherrer equation, we calculated the average crystallite sizes for Ni/G5-10, Ni/G5-15, Ni/G10-15, and Ni/G10-5 based on the Ni (111) peak, yielding values of 31.3 nm, 29.2 nm, 28.7 nm, and 31.3 nm, respectively, which was larger than that of Ni/G10 and Ni/G0-10 in our previous work [32]. As Ni/G5-10 had the same size as Ni/G10-5, we concluded that the grain size was not only related to the upper layer, but the average size of the two layers.

2.2. XPS Analysis

As to Ni/G5-10, the XPS spectrum of Ni 2p, C 1s, and O 1s is shown in Figure 2a. To accurately identify the chemical phases presented in the samples, peak fitting analysis was performed on the Ni 2p spectrum. As shown in Figure 2b, the main peaks of Ni 2p_{3/2} were located at approximately 856 eV, 857.5 eV, and 862.5 eV, which corresponded to the nickel compounds such as Ni(OH)₂, NiSO₄, and NiCl₂, indicating that nickel existed in a divalent state [33–35]. Additionally, a Ni(0) peak appeared around 852 eV, confirming the presence of metallic nickel in the coating [36]. The OH[−], SO₄^{−2}, and Cl[−] ions might be derived from the plating solution used during coating preparation.

2.3. Tafel Analysis

The Tafel curves for the Ni/G composite coatings in pH 3 sulfuric acid are shown in Figure 3, with testing temperatures of 50 °C and 80 °C, respectively. The data for corrosion potential (E_{corr}), corrosion current (I_{corr}), and corrosion rate (V_{corr}) obtained from the Tafel analysis are presented in Table 1. E_{corr} is defined as the intersection of the anodic and cathodic polarization curves, indicating the self-corrosion potential of the coating. I_{corr} is a kinetic parameter obtained through extrapolation [37]. According to the corrosion rate equation, the corrosion rate coefficient is derived from the corrosion current.

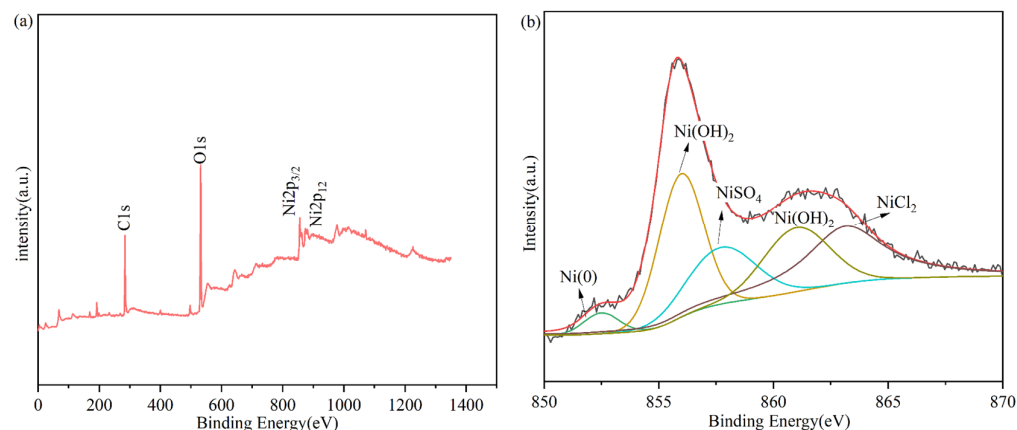


Figure 2. XPS of Ni/G5-10 (a) and Ni 2p (b) fitting spectrum.

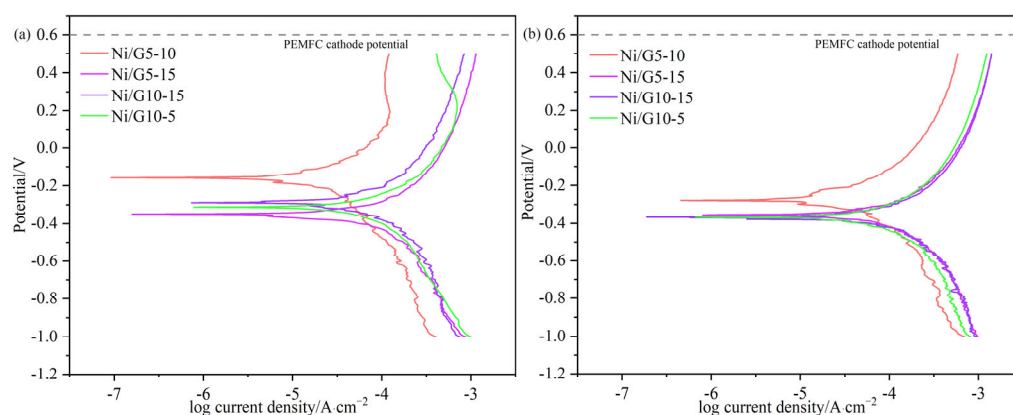


Figure 3. Tafel curves for Ni/G composite coatings tested at 50 °C (a) and 80 °C (b).

Table 1. Tafel polarization parameters for Ni/G composite coatings at 50 °C and 80 °C.

	I_{corr} ($\mu\text{A}\cdot\text{cm}^{-2}$)		E_{corr} (V)		V_{corr} ($\times 10^{-2}$ mm \cdot y $^{-1}$)	
	50 °C	80 °C	50 °C	80 °C	50 °C	80 °C
Ni/G5-10	26.14	43.80	−0.159	−0.278	0.283	0.473
Ni/G5-15	52.51	62.25	−0.348	−0.355	0.568	0.673
Ni/G10-15	66.27	71.70	−0.289	−0.366	0.716	0.775
Ni/G10-5	73.54	81.14	−0.312	−0.368	0.795	0.877

As shown in Table 1, with increasing temperature, all samples exhibited an increase in I_{corr} , a more negative shift in E_{corr} , and an increased V_{corr} , indicating that higher temperatures correlated with more severe corrosion and accelerated corrosion rates. At 50 °C, the gradient coatings Ni/G5-10, Ni/G5-15, and Ni/G10-15 outperformed Ni/G10-5. Ni/G5-10 exhibited the lowest I_{corr} and the most positive E_{corr} , with the values of $26.14 \mu\text{A}\cdot\text{cm}^{-2}$ and -0.159 V, respectively. Compared to the values of Ni/G10-5, its I_{corr} decreased by 64.45% and E_{corr} improved by 24.46%. The same trend was observed at 80 °C.

2.4. Constant Potential Analysis

The stability of Ni/G coatings was tested at a constant potential of 0.6 V and 50 °C, with the current versus time changed shown in Figure 4. All samples quickly reached a stable current state within the first few minutes, exhibiting no significant fluctuations over 120 min and thus indicating a rapid self-repair process of the materials [38]. The current densities of Ni/G5-10, Ni/G5-15, Ni/G10-15, and Ni/G10-5 are 0.12, 0.38, 0.42, and $0.58 \text{ mA}\cdot\text{cm}^{-2}$, respectively. Among them, Ni/G5-10 has a positive stable point voltage, indicating that the corrosion resistance is better, which has the same rule as Tafel analysis.

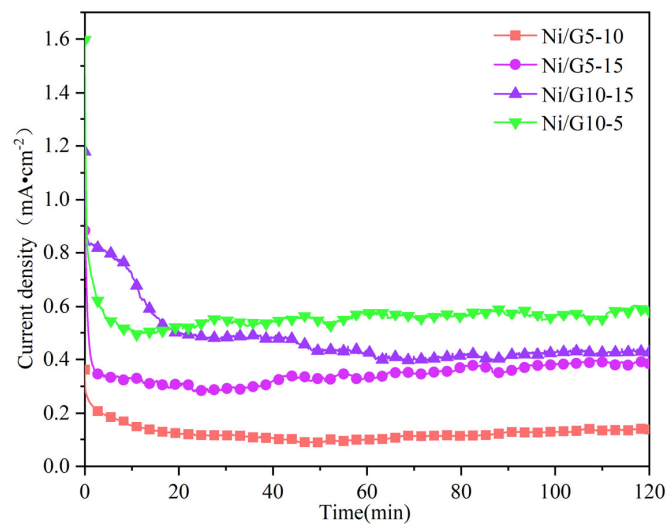


Figure 4. Constant potential curve for Ni/G composite coatings.

2.5. EIS Analysis

Figure 5 presents the results of all samples tested in a 0.5 M H_2SO_4 solution with 2 ppm HF at 50 °C. As shown in Figure 5a, the Nyquist plots for all coatings exhibit a semi-circular arc, indicating a similar corrosion mechanism across the samples. Among them, Ni/G5-10 displays the largest impedance semicircle radius. The Randles circuit was chosen as the equivalent circuit, as illustrated in Figure 5b, which consists of solution resistance (R_s), coating resistance (R_{coat}), and a constant phase element (C_{coat}). The fitted values are summarized in Table 2. Compared to the uncoated foam nickel ($R_{\text{coat}} = 5.27 \Omega \cdot \text{cm}^2$) [21], the Ni/G composite coatings exhibit significantly higher R_{coat} values, indicating better corrosion resistance. Notably, the gradient coating Ni/G5-10 has the highest R_{coat} , demonstrating the strongest corrosion resistance among the samples.

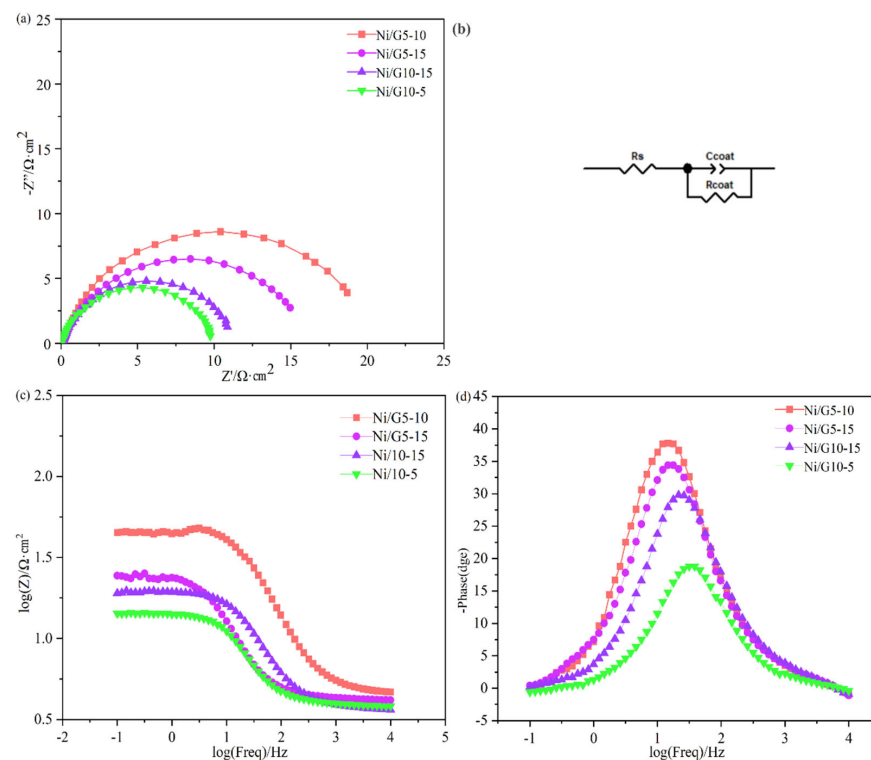


Figure 5. EIS analysis results for Ni/G composite coatings: (a) Nyquist impedance plots; (b) equivalent circuit; (c,d) Bode impedance plots.

Table 2. EIS fitting results for Ni/G composite coatings.

Samples	R_s ($\Omega \cdot \text{cm}^2$)	C_{coat}		R_{coat} ($\Omega \cdot \text{cm}^2$)
		$C_{\text{coat-T}}$	$C_{\text{coat-P}}$	
5–10	4.28	2.21×10^{-3}	0.87	19.79
5–15	3.72	1.06×10^{-3}	0.85	16.09
10–15	3.02	2.8×10^{-3}	0.88	12.26
10–5	8.35	1.05×10^{-3}	0.91	9.78

In Figure 5c,d, all Bode plots display high-frequency (10^2 – 10^4 Hz), mid-frequency (10^1 – 10^2 Hz), and low-frequency (10^{-1} – 10^1 Hz) regions, which correspond to the corrosion processes at the coating surface, within the coating system, and at the metal/coating interface, respectively. In Figure 5c, Ni/G5-10 shows the highest $\log(Z)$ values across the entire frequency range, indicating the best corrosion resistance of the coating. In Figure 5d, the phase angles for Ni/G5-10, Ni/G5-15, and Ni/G10-15 are all greater than that of Ni/G10-5, which correlates with improved corrosion resistance.

2.6. SEM Analysis

The stability of the Ni/G composite coatings was studied by testing for 8 h at a constant potential of 0.6 V. The SEM images before and after the test are shown in Figure 6. As depicted in Figure 6a–d, the surface of the composite coatings is smooth and uniform, with no significant aggregation observed. In our previous work, the grain sizes of the coatings that were electrodeposited at 5, 10, and 15 $\text{mA} \cdot \text{cm}^{-2}$, were found to be 37.0 nm, 33.2 nm, and 24.9 nm, respectively. In the schematic diagrams, colored particles were used to represent the grains in the hierarchical coatings. The graphene layer covered the surface of nickel ions, hindering further growth during the electrodeposition process while providing more nucleation sites for the reduction of nickel ions, resulting in smaller and more uniform composite coatings [39,40]. After the corrosion test, more sheet graphene was exposed, as shown in Figure 6a–d.

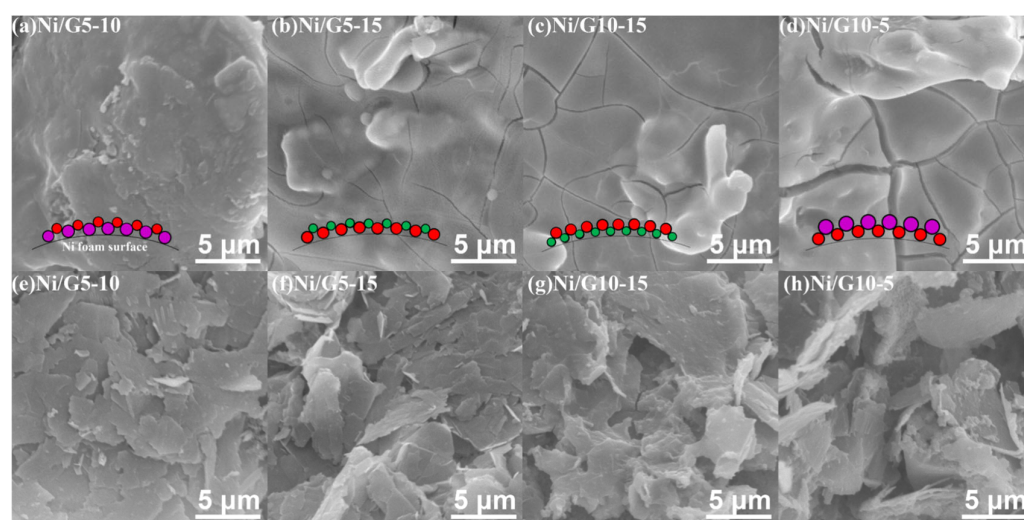


Figure 6. SEM images of Ni/G composite coatings and schematic diagrams with colored particles for hierarchical coatings before (a–d) and after (e–h) the 8h corrosion (purple, red, and green represents grains electrodeposited at 5, 10, and 15 $\text{mA} \cdot \text{cm}^{-2}$, respectively).

2.7. EDS Analysis

The atomic composition of the main elements in the Ni/G5-10 composite coating before and after corrosion was analyzed using energy dispersive spectroscopy (EDS). As shown in Figure 7a, the presence of carbon confirmed the incorporation of graphene into the coating, which at the same time aided the reduction of nickel ions during the electrodeposition process, leading to the formation of metallic nickel [41]. Higher oxygen content might be attributed to the oxidation reaction, especially that of the nano-particles, occurring at the coating surface.

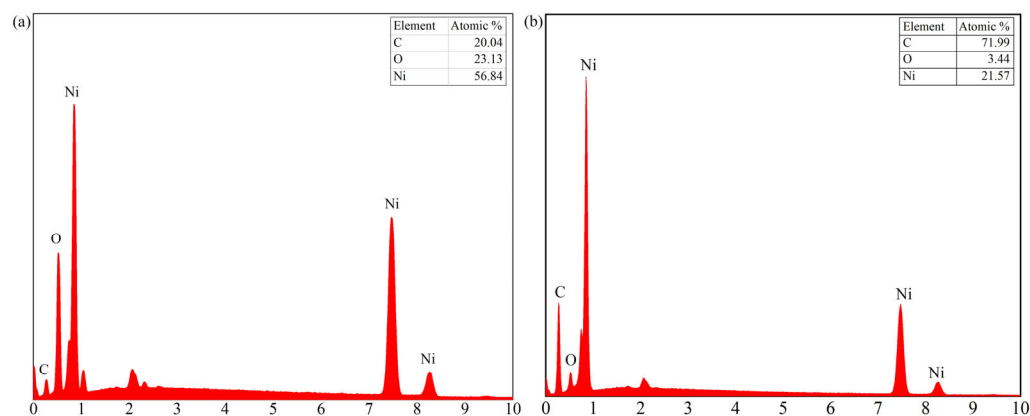


Figure 7. EDS of Ni/G5-10 before (a) and after (b) 8 h corrosion.

As shown in Figure 7b, after 8 h of corrosion, the carbon content in the coating increased significantly from 20.04% to 71.99%, while the nickel content decreased from 56.84% to 21.57%. During the corrosion process, metallic nickel gradually dissolved and converted to Ni^{2+} ions, which then entered into the solution. In contrast, graphene, with superior corrosion resistance and stability, played a protective role on the surface.

2.8. ICR Analysis

In addition to corrosion resistance, the interfacial contact resistance (ICR) is also a critical parameter for bipolar plates. A high ICR leads to additional resistance to current flow within the cell, resulting in reduced efficiency and negatively impacting the fuel cell's output power. In Figure 8a, the values of all the samples decreased with the pressure. Ni/G5-10 exhibited the lowest ICR value, which might be attributed to the formation of a uniform and dense coating. In Figure 8b, the value at a pressure of $150 \text{ N}\cdot\text{cm}^{-2}$ (the typical assembly pressure for PEMFCs) of Ni/G5-10 was $7.16 \text{ m}\Omega\cdot\text{cm}^2$, which met the 2025 DOE standard requirement ($<10 \text{ m}\Omega\cdot\text{cm}^2$) [17].

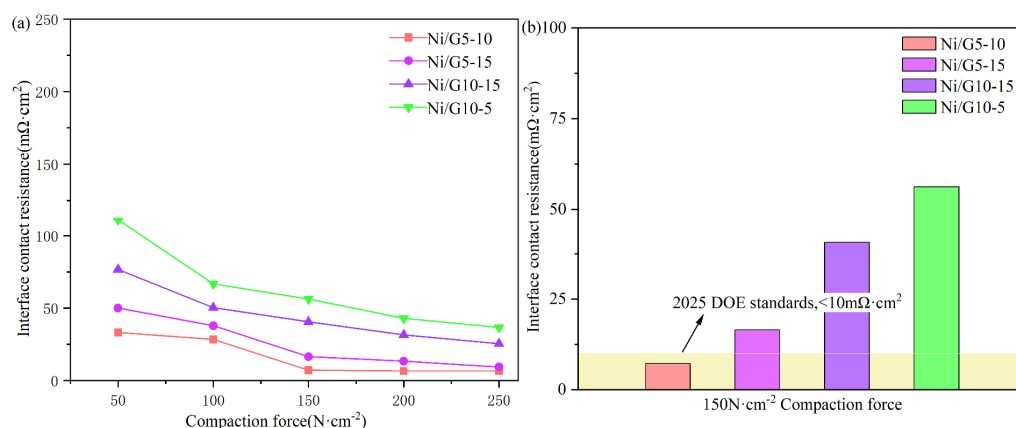


Figure 8. ICR of Ni/G composite coatings under various compaction force (a) and the values under $150 \text{ N}\cdot\text{cm}^{-2}$ (b).

3. Experimental

3.1. Electrodeposition

The foam nickel used in the experiment was obtained from Kunshan Green Creation Electronics Technology Co., Ltd. (Kunshan, China), with a thickness of 1 mm and a pore diameter around 600 μm . Prior to electrodeposition, the foam nickel underwent pretreatment and activation [42]. The Ni/G composite coating bath consisted of 12.9 $\text{g}\cdot\text{L}^{-1}$ $(\text{SO}_3\text{NH}_2)_2\cdot 4\text{H}_2\text{O}$ (Shanghai Macklin Biochemical Technology Co., Ltd., Shanghai, China), 9.51 $\text{g}\cdot\text{L}^{-1}$ $\text{NiCl}_2\cdot 6\text{H}_2\text{O}$ (Shanghai Macklin Biochemical Technology Co., Ltd., Shanghai, China), 40 $\text{g}\cdot\text{L}^{-1}$ H_3BO_3 (Shanghai Macklin Biochemical Technology Co., Ltd., Shanghai, China), 0.05 $\text{g}\cdot\text{L}^{-1}$ $\text{C}_{12}\text{H}_{25}\text{SO}_4\text{Na}$ (Shanghai Macklin Biochemical Technology Co., Ltd., Shanghai, China), 10 $\text{g}\cdot\text{L}^{-1}$ $\text{C}_6\text{H}_5\text{Na}_3\text{O}_7$ (Shanghai Macklin Biochemical Technology Co., Ltd., Shanghai, China), 0.048 $\text{g}\cdot\text{L}^{-1}$ graphene (Shanghai Macklin Biochemical Technology Co., Ltd., Shanghai, China) powder (97%), and 100 $\text{mL}\cdot\text{L}^{-1}$ $\text{C}_5\text{H}_9\text{NO}$. In the three-electrode system using a CHI660E (Shanghai Chenhua Co., Ltd., Shanghai, China), the foam nickel served as the cathode while a nickel plate (99.9%, Chen Shuo Co., Ltd., Fuzhou, China) acted as the anode. The electrodeposition was conducted at a temperature of 328 K for a duration of 20 min, under various current densities: 5, 10, and 15 $\text{mA}\cdot\text{cm}^{-2}$. The hierarchical structure was obtained by depositing under two current densities with each current deposited for 10 min. The coated samples were named Ni/G5-10, Ni/G5-15, Ni/G10-15, and Ni/G10-5, respectively. Following electrodeposition, the samples were dried in an oven at 60 $^\circ\text{C}$ for 8 h.

3.2. Morphology Investigation

X-ray diffraction (XRD) was tested using an X-ray diffractometer model (Kuraray Co., Ltd., Tokyo, Japan) KYOWAGLAS-XA H-12 using Cu $\text{K}\alpha$ radiation at operating voltages of 40 mA, 40 kV, and $2\theta = 5\sim 80^\circ$.

X-ray photoelectron spectroscopy (XPS) analysis was performed using Horiba LabRAM HR X-ray (HORIBA SAS Co., Ltd., Palaiseau, France) photoelectron spectroscopy.

Field emission scanning electron microscopy (SEM) was conducted using a Phenom Pro X model from Funa Scientific Instruments (Shanghai, China) Co., Ltd., with an applied voltage set between 10 and 15 kV. Prior to testing, the samples were gold-coated and then placed on the microscope sample stage for analysis.

The elements in the samples were identified and quantitatively analyzed by EDS detection. In this study, SU1510 (Hitachi High-tech Company, Tokyo, Japan) was used to test the foam metal sample. The voltage was set at 15.0 kV, the working distance was 15 mm, and the mode was selected as surface scan. The content and distribution of carbon, oxygen, and nickel were the main areas of study.

The experimental method of interface contact resistance (ICR) was the same as Liu et al.'s [24]. The test sample was placed between two sheets of carbon paper, then between copper electrodes, and the two electrodes were fixed on the TS-C40L-B (Tycoway Automation Systems Co., Ltd., Shenzhen, China) press, and 3 mA constant current was output through the MP3030D (MAISHENG Co., Ltd., Shenzhen, China) voltage regulator power supply. At the same time, the press applied pressure from small to large, and the ICR value of each sample was obtained under different pressures.

3.3. Corrosion Resistance Measurements

Electrochemical testing was conducted in a traditional three-electrode configuration [22], with a platinum sheet (Chuxi Industry Co., Ltd., Shanghai, China) as the counter electrode, an Ag/AgCl (Chuxi Industry Co., Ltd., Shanghai, China) reference electrode, and a working electrode comprising a foam nickel with an area of 1 cm^2 . The Tafel test was performed in H_2SO_4 solution with pH = 3, the voltage range was set to -1 to 0.5, and the scan rate was 1 $\text{mV}\cdot\text{s}^{-1}$. A potentiostatic test was performed at 50 $^\circ\text{C}$, with a voltage of 0.6 V and air pumped into the sulfuric acid solution to simulate the fuel cell cathode environment. The electrochemical impedance spectroscopy (EIS) test was performed at

50 °C and in a 2 ppm HF (Shanghai Macklin Biochemical Technology Co., Ltd., Shanghai, China) solution containing $0.5 \text{ mol}\cdot\text{L}^{-1}$ H_2SO_4 (Shanghai Macklin Biochemical Technology Co., Ltd., Shanghai, China), with a set frequency range from 10 kHz to 0.1 Hz and an amplitude voltage of 10 mV.

4. Conclusions

This study successfully fabricated Ni/G composite coatings with hierarchical structures on foam nickel using electrodeposition under different current densities. During the co-deposition of Ni and graphene, the effect of the grain size in the inner layer and the outer layer was discussed. It was found that Ni/G5-10, with larger inner size and a middle outer size, exhibited the best corrosion performance, with the lowest dynamic and steady-state corrosion currents, as well as the highest coating resistance. Compared with the coatings obtained under the steady and gradient current, the hierarchically electrodeposited coating improved the stability of the foam metals. Although the grain size was larger than that of the former coatings, the composite of NiO and graphene covered the surface of metal foam and formed a uniform and dense protective film. Moreover, its ICR value was $7.16 \text{ m}\Omega\cdot\text{cm}^2$, with a 11.8% reduction relative to the US DOE 2025 goal, resulting in lower ohmic resistance and less heat power in the fuel cell operation.

Author Contributions: Conceptualization, Y.X., G.H. and B.F.; Methodology, Q.Z. and C.S.; Formal analysis, Q.Z.; Investigation, Q.Z. and C.S.; Writing—original draft, Y.X. and Q.Z.; Writing—review & editing, Y.X.; Supervision, Y.X., G.H. and B.F.; Project administration, G.H. All authors have read and agreed to the published version of the manuscript.

Funding: This research received no external funding.

Data Availability Statement: The original contributions presented in the study are included in the article, further inquiries can be directed to the corresponding authors.

Conflicts of Interest: The authors declare no conflict of interest.

References

1. Gayen, D.; Chatterjee, R.; Roy, S. A review on environmental impacts of renewable energy for sustainable development. *Int. J. Environ. Sci. Technol.* **2024**, *21*, 5285–5310. [[CrossRef](#)]
2. Stergaard, P.A.; Duic, N.; Noorollahi, Y. Renewable energy for sustainable development. *Renew. Energy* **2022**, *199*, 1145–1152. [[CrossRef](#)]
3. Ahmed, H.; Adebayo, P.; Ahmed, M.; Arbab, A.I. Hydrogen fuel cell technology: Benefits, challenges, and future potential. *J. Energy Technol. Policy* **2023**, *13*, 2224–3232.
4. Aminudin, M.; Kamarudin, S.; Lim, B.; Majilan, E.; Masdar, M.; Shaari, N. An overview: Current progress on hydrogen fuel cell vehicles. *Int. J. Hydrogen Energy* **2023**, *48*, 4371–4388. [[CrossRef](#)]
5. Cai, F.; Cai, S.; Tu, Z. Proton exchange membrane fuel cell (PEMFC) operation in high current density (HCD): Problem, progress and perspective. *Energy Convers. Manag.* **2024**, *307*, 118348. [[CrossRef](#)]
6. Hermann, A.; Chaudhuri, T.; Spagnol, P. Bipolar plates for PEM fuel cells: A review. *Int. J. Hydrogen Energy* **2005**, *30*, 1297–1302. [[CrossRef](#)]
7. Liu, R.; Jia, Q.; Zhang, B.; Lai, Z.; Chen, L. Protective coatings for metal bipolar plates of fuel cells: A review. *Int. J. Hydrogen Energy* **2022**, *47*, 22915–22937. [[CrossRef](#)]
8. Kloess, J.P.; Wang, X.; Liu, J.; Shi, Z.; Guessous, L. Investigation of bio-inspired flow channel designs for bipolar plates in proton exchange membrane fuel cells. *J. Power Sources* **2009**, *188*, 132–140. [[CrossRef](#)]
9. Liu, Q.; Lan, F.; Zeng, C.; Chen, J.; Wang, J. A review of proton exchange membrane fuel cell's bipolar plate design and fabrication process. *J. Power Sources* **2022**, *538*, 231543. [[CrossRef](#)]
10. Kuan, Y.D.; Wang, C.K.; Yang, C.; Lee, P.C.; Siao, Y.S.; Lee, C.Y. Fuel cell stack design using carbon fiber composites. *Sens. Mater.* **2020**, *32*, 4233–4244. [[CrossRef](#)]
11. Gomez Sanchez, A.; Franco Luján, V.A.; Alfaro López, H.M.; Hernández-Sánchez, L.; Cruz-Martínez, H.; Medina, D.I. carbon material-reinforced polymer composites for bipolar plates in polymer electrolyte membrane fuel cells. *Polymers* **2024**, *16*, 671. [[CrossRef](#)] [[PubMed](#)]
12. Wenkai, L.; Zhiyong, X.; Haodong, Z. Current status of research on composite bipolar plates for proton exchange membrane fuel cells (PEMFCs): Nanofillers and structure optimization. *RSC Adv.* **2024**, *14*, 7172–7194. [[PubMed](#)]

13. Wang, X.Z.; Fan, H.Q.; Muneshwar, T.; Cadien, K.; Luo, J.L. Balancing the corrosion resistance and through-plane electrical conductivity of cr coating via oxygen plasma treatment. *J. Mater. Sci. Technol.* **2021**, *61*, 75–84.
14. McCay, K.; Kongstein, O.E.; Oedegaard, A.; Barnett, A.O.; Seland, F. Soldering a gas diffusion layer to a stainless steel bipolar plate using metallic tin. *Int. J. Hydrogen Energy* **2018**, *43*, 9006–9014.
15. Chanda, U.K.; Behera, A.; Roy, S.; Pati, S. Evaluation of Ni-Cr-P coatings electrodeposited on low carbon steel bipolar plates for polymer electrolyte membrane fuel cell. *Int. J. Hydrogen Energy* **2018**, *43*, 23430–23440.
16. Pukha, V.; Glukhov, A.; Belmesov, A.; Kabachkov, E.; Khodos, I.; Khadem, M.; Kim, D.E.; Karaseov, P. Corrosion-resistant nanostructured carbon-based coatings for applications in fuel cells based on bipolar plates. *Vacuum* **2023**, *218*, 112643.
17. Li, S.; Jin, R.; Li, S. High corrosion resistance and conductivity of Al₂O₃/CrN coating for metal bipolar plates in PEMFCs: Al₂O₃ hinders CrN columnar crystals growth. *Int. J. Hydrogen Energy* **2024**, *50*, 805–816. [[CrossRef](#)]
18. Kim, Y.S.; Lee, I.S.; Choi, J.Y.; Jun, S.; Kim, D.; Cha, B.C.; Kim, D.W. Corrosion behavior of niobium-coated 316L stainless steels as metal bipolar plates for polymer electrolyte membrane fuel cells. *Materials* **2021**, *14*, 4972. [[CrossRef](#)]
19. Chauhan, D.S.; Quraishi, M.; Ansari, K.; Saleh, T.A. Graphene and graphene oxide as new class of materials for corrosion control and protection: Present status and future scenario. *Prog. Org. Coat.* **2020**, *147*, 105741.
20. Wang, Z.; Xia, Y.; Lei, H.; Hu, G. Enhanced corrosion resistance of Ni/Sn nano-electrodeposited metal foam for flow field application in simulated PEMFC cathode environment. *Int. J. Hydrogen Energy* **2022**, *47*, 35412–35422. [[CrossRef](#)]
21. Ollik, K.; Lieder, M. Review of the application of graphene-based coatings as anticorrosion layers. *Coatings* **2020**, *10*, 883. [[CrossRef](#)]
22. Lee, Y.H.; Li, S.M.; Tseng, C.J.; Su, C.Y.; Lin, S.C.; Jhuang, J.W. Graphene as corrosion protection for metal foam flow distributor in proton exchange membrane fuel cells. *Int. J. Hydrogen Energy* **2017**, *42*, 22201–22207. [[CrossRef](#)]
23. Wang, J.; Min, L.; Fang, F.; Zhang, W.; Wang, Y. Electrodeposition of graphene nano-thick coating for highly enhanced performance of titanium bipolar plates in fuel cells. *Int. J. Hydrogen Energy* **2019**, *44*, 16909–16917. [[CrossRef](#)]
24. Liu, Y.; Min, L.; Zhang, W.; Wang, Y. High-performance graphene coating on titanium bipolar plates in fuel cells via cathodic electrophoretic deposition. *Coatings* **2021**, *11*, 437. [[CrossRef](#)]
25. Yu, F.; Wang, K.; Cui, L. Vertical-graphene-reinforced titanium alloy bipolar plates in fuel cells. *Adv. Mater.* **2022**, *34*, 2110565.
26. Pandey, U.; Singh, A.; Sharma, C. Development of anti-corrosive novel nickel-graphene oxide-polypyrrole composite coatings on mild steel employing electrodeposition technique. *Synth. Met.* **2022**, *290*, 117135. [[CrossRef](#)]
27. Mu, J.; Gao, F.; Cui, G.; Wang, S.; Tang, S.; Li, Z. A comprehensive review of anticorrosive graphene-composite coatings. *Prog. Org. Coat.* **2021**, *157*, 106321.
28. Rekha, M.; Kumar, M.P.; Srivastava, C. Electrochemical behaviour of chromium-graphene composite coating. *RSC Adv.* **2016**, *6*, 62083–62090.
29. Kumar, M.P.; Singh, M.P.; Srivastava, C. Electrochemical behavior of Zn-graphene composite coatings. *RSC Adv.* **2015**, *5*, 25603–25608.
30. Jabbar, A.; Yasin, G.; Khan, W.Q.; Anwar, M.Y.; Korai, R.M.; Nizam, M.N.; Muhyodin, G. Electrochemical deposition of nickel graphene composite coatings: Effect of deposition temperature on its surface morphology and corrosion resistance. *RSC Adv.* **2017**, *7*, 31100–31109.
31. Sun, C.; Hu, G.; Cao, L.; Pan, T.; Guo, C.; Xia, Y. Ni/graphene coating for enhanced corrosion resistance of metal foam flow field in simulated pemfc cathode environment. *ACS Omega* **2024**, *9*, 29797–29804. [[CrossRef](#)] [[PubMed](#)]
32. Yigit, O.; Dikici, B.; Senocak, T.C.; Ozdemir, N. One-step synthesis of nano-hydroxyapatite/graphene nanosheet hybrid coatings on Ti6Al4V alloys by hydrothermal method and their in-vitro corrosion responses. *Surf. Coat. Technol.* **2020**, *394*, 125858. [[CrossRef](#)]
33. Nesbitt, H.; Legrand, D.; Bancroft, G. Interpretation of Ni2p XPS spectra of Ni conductors and Ni insulators. *Phys. Chem. Miner.* **2000**, *27*, 357–366. [[CrossRef](#)]
34. Saldan, I.; Lewin, E.; Dobrovetska, O.; Karlsson, D.; Bilan, O.; Kunttyi, O. Surface analysis of nickel nanomaterials electrodeposited on graphite surface. *Micro Nano Lett.* **2019**, *14*, 1233–1237. [[CrossRef](#)]
35. Michał, G.; Mohammad, A.; Gregory, J. Surface science and electrochemical analysis of nickel foams. *ACS Appl. Mater. Interfaces* **2012**, *4*, 3012–3021.
36. Prieto, P.; Nistor, V.; Nouneh, K. XPS study of silver, nickel and bimetallic silver-nickel nanoparticles prepared by seed-mediated growth. *Appl. Surf. Sci.* **2012**, *258*, 8807–8813. [[CrossRef](#)]
37. Siddaiah, A.; Kumar, P.; Henderson, A.; Misra, M.; Menezes, P.L. Surface energy and tribology of electrodeposited Ni and Ni-graphene coatings on steel. *Lubricants* **2019**, *7*, 87. [[CrossRef](#)]
38. Wang, H.; Sweikart, M.A.; Turner, J.A. Stainless steel as bipolar plate material for polymer electrolyte membrane fuel cells. *J. Power Sources* **2003**, *115*, 243–251. [[CrossRef](#)]
39. Li, X.; Shen, Q.; Zhang, Y.; Wang, L.; Nie, C. Wear behavior of electrodeposited nickel/graphene composite coating. *Diam. Relat. Mater.* **2021**, *119*, 108589. [[CrossRef](#)]
40. Kumar, C.P.; Venkatesha, T.; Shabadi, R. Preparation and corrosion behavior of Ni and Ni-graphene composite coatings. *Mater. Res. Bull.* **2013**, *48*, 1477–1483. [[CrossRef](#)]

41. Algul, H.; Tokur, M.; Ozcan, S.; Uysal, M.; Cetinkaya, T.; Akbulut, H.; Alp, A. The effect of graphene content and sliding speed on the wear mechanism of nickel-graphene nanocomposites. *Appl. Surf. Sci.* **2015**, *359*, 340–348. [[CrossRef](#)]
42. Li, N.; Xu, H.; Li, X. Tribological properties and corrosion resistance of porous structure Ni-Mo/ZrO₂ Alloys. *Coatings* **2020**, *10*, 767. [[CrossRef](#)]

Disclaimer/Publisher's Note: The statements, opinions and data contained in all publications are solely those of the individual author(s) and contributor(s) and not of MDPI and/or the editor(s). MDPI and/or the editor(s) disclaim responsibility for any injury to people or property resulting from any ideas, methods, instructions or products referred to in the content.